AGU PUBLICATIONS

JGR

Journal of Geophysical Research: Oceans

RESEARCH ARTICLE

10.1002/2014JC010412

Key Points:
- A shallow-water wind stress parameterization has yet to be developed
- Nearshore wind stress is significantly underestimated by conventional methods
- This has implications for studies and simulations of nearshore dynamics

Correspondence to:
D. G. Ortiz-Suslow,
dortiz-suslow@rsmas.miami.edu

Citation:
Ortiz-Suslow, D. G., B. K. Haus, N. J. Williams, N. J. M. Laxague, A. J. H. M. Reniers, and H. C. Graber (2015), The spatial-temporal variability of air-sea momentum fluxes observed at a tidal inlet, *J. Geophys. Res. Oceans*, *120*, 660–676, doi:10.1002/2014JC010412.

Received 29 AUG 2014
Accepted 7 JAN 2015
Accepted article online 19 JAN 2015
Published online 5 FEB 2015

The spatial-temporal variability of air-sea momentum fluxes observed at a tidal inlet

D. G. Ortiz-Suslow[1], B. K. Haus[1], N. J. Williams[1], N. J. M. Laxague[1], A. J. H. M. Reniers[2], and H. C. Graber[1]

[1]Rosenstiel School of Marine and Atmospheric Science, University of Miami, Miami, Florida, USA, [2]Civil Engineering and Geosciences, Delft University of Technology, Delft, Netherlands

Abstract Coastal waters are an aerodynamically unique environment that has been little explored from an air-sea interaction point of view. Consequently, most studies must assume that open ocean-derived parameterizations of the air-sea momentum flux are representative of the nearshore wind forcing. Observations made at the New River Inlet in North Carolina, during the Riverine and Estuarine Transport experiment (RIVET), were used to evaluate the suitability of wind speed-dependent, wind stress parameterizations in coastal waters. As part of the field campaign, a small, agile research vessel was deployed to make high-resolution wind velocity measurements in and around the tidal inlet. The eddy covariance method was employed to recover direct estimates of the 10 m neutral atmospheric drag coefficient from the three-dimensional winds. Observations of wind stress angle, near-surface currents, and heat flux were used to analyze the cross-shore variability of wind stress steering off the mean wind azimuth. In general, for onshore winds above 5 m/s, the drag coefficient was observed to be two and a half times the predicted open ocean value. Significant wind stress steering is observed within 2 km of the inlet mouth, which is observed to be correlated with the horizontal current shear. Other mechanisms such as the reduction in wave celerity or depth-limited breaking could also play a role. It was determined that outside the influence of these typical coastal processes, the open ocean parameterizations generally represent the wind stress field. The nearshore stress variability has significant implications for observations and simulations of coastal transport, circulation, mixing, and general surf-zone dynamics.

1. Introduction

The nearshore is a dynamic and complex environment where many physical processes converge in relatively shallow depths. In addition to the physical importance, the ocean's coasts hold significant implications for economic and human health-focused coastal management. This motivates the development of sophisticated coastal models to simulate current and wave fields, as well as sediment and tracer transport. For example, *Feng et al.* [2013] used a physics-based nearshore model, coupled with a microbe transport-decay module, to hindcast fecal indicator bacteria levels at a popular South Florida beach. *Fujimura et al.* [2014] used a biological-physical coupled model to simulate the cross-surf zone transport of larval invertebrates. They found that the transport was significantly dependent on the whether or not there was onshore wind forcing included in the simulation. Like many nearshore modeling platforms, these studies maintained a simple, open ocean-derived wind stress parameterization, which is at best a simplistic, first-order approximation [*Shabani et al.*, 2014].

For decades, air-sea momentum flux research has focused on developing a parameterization scheme that can be universally applied over a wide range of wind speeds and sea states. While this has yet to be fully realized, the important role that the wind stress plays in a number of physical processes (e.g., wind-wave generation, surface transport, and mixing) necessitates the continued effort to develop a complete wind forcing model that may be applied from the ocean basins to the coastal shorelines.

Longstanding seminal work reported by *Charnock* [1955] led to the general principle that the wind stress increases with wind speed, where the shear stress is taken as,

$$\tau = \rho_a u_*^2 = \rho C_z |U_z|^2 \quad (1)$$

here u_* and U_z are the friction velocity (or wind shear velocity) and the wind speed (referenced to some height, z, above the air-water interface), respectively. The air density is ρ_a, and C_z is the dimensionless

aerodynamic drag coefficient. Decades of study have been dedicated to characterizing this coefficient as some function of wind speed and sea state, but the exact nature of C_z remains elusive.

Subsequent investigations used a variety of methods to confirm the general nature of the Charnock model, i.e., the drag coefficient increases linearly with wind speed [*Smith and Banke*, 1975; *Garratt*, 1977]. This relation was later piece-wise defined for wind speeds generally between 5 and 25 m/s [*Smith*, 1980; *Large and Pond*, 1981]. However, significant scatter existed in the literature for low and high wind regimes. Later work revealed a sharp increase in the atmospheric drag for winds approaching 0 m/s [*Edson et al*., 2013], which *Zhu and Furst* [2013] demonstrate cannot be explained by Monin-Obukhov Similarity (MOS) Theory [*Monin and Obukhov*, 1954]. Among limited field observations, *Donelan et al*. [2004] used laboratory data to show that the drag diverges from linearity at extremely high wind speeds (∼30–35 m/s).

Much of this early work assumed a wind speed-dependent roughness formulation,

$$z_0 = m u_*^2 / g \tag{2}$$

where m is some dimensionless constant and g is the gravitational acceleration. However, there has been a significant amount of work done to relate the roughness length, z_0, to the wave field underneath the atmospheric boundary layer. Since being first proposed by *Kitaigorodskii and Volkov* [1965], some investigators have sought to relate the atmospheric drag to both the wind and swell-seas underneath the atmospheric boundary layer [e.g., *Donelan*, 1990; *Anctil and Donelan*, 1996; *Drennan et al*., 1999; *Sahleé et al*., 2012]. *Edson et al*. [2013] provides a detailed review of the methods used to parameterize C_z as some function of wind speed or sea state.

The citations referenced above provide the breadth of techniques and platforms that have been used to measure air-sea momentum fluxes in the field and in the laboratory. Towers, moored, and floating buoys, ships, and wind-wave flumes have all been used in the concerted effort to better understand air-sea turbulent exchange in a wide range of ocean and atmospheric conditions. Much of the prior work only considered the open ocean, deep water regime where the seas were near full development [*Anctil and Donelan*, 1996] and the wind stress was assumed to be aligned with the wind vector [*Geernaert*, 1988]. However, *Zhang et al*. [2009] reported that in the presence of strong horizontal current shear, the peak of the wind sea directional spectrum and the wind stress vector were steered off the mean wind direction. Generally, in equation (1), the friction velocity is defined as, $u_* = -\overline{u_i u_j}$, where the only component of the Reynolds stress considered is the component aligned with the wind direction, and off-wind stresses are assumed negligible [*Smith*, 1980].

This paper presents results from a field campaign, the Riverine and Estuarine Transport experiment part 1 (RIVET I), which took place at the New River Inlet (NRI), North Carolina. Direct measurements of the wind stress were made from a small, agile research vessel that captured the spatial and temporal variability of the momentum fluxes near this tidal inlet. This study area provides a unique venue for air-sea momentum flux investigation and the results of this study will highlight the degree to which open ocean drag coefficient parameterizations are appropriate as an approximation to the wind stress in the nearshore.

There exists a gap in the atmospheric boundary layer literature detailing the role of shallow-water processes on the momentum flux, including current shear [*Zhang et al*., 2009], intense wave breaking and decreased wave celerity during shoaling [*Shabani et al*., 2014], and slanting fetch [*Ardhuin et al*., 2007]. To the authors' knowledge, the suitability of open ocean-derived methods for use in coastal waters has yet to be fully tested. Therefore, the aim of this study is to extend our understanding of air-sea momentum fluxes to the currently underexplored coastal environment [*Edson et al*., 2013]. Large-scale processes (e.g., incident wave height and regional circulation) are independent of locally variable wind stresses. However, the nearshore wind forcing has been shown to affect littoral transport [*Fujimura et al*., 2014] and circulation patterns [*Wargula et al*., 2014]. A more realistic wind stress parameterization could explain the variability in both nearshore observations and simulations that generally relied on an open ocean drag coefficient.

2. Methods

2.1. Field Site

The RIVET 1 experiment took place at NRI from April to June 2012. NRI is a natural, sandy-bottom tidal inlet, free from jetties or break waters, on the southeast coast of North Carolina located at 34.528°N and

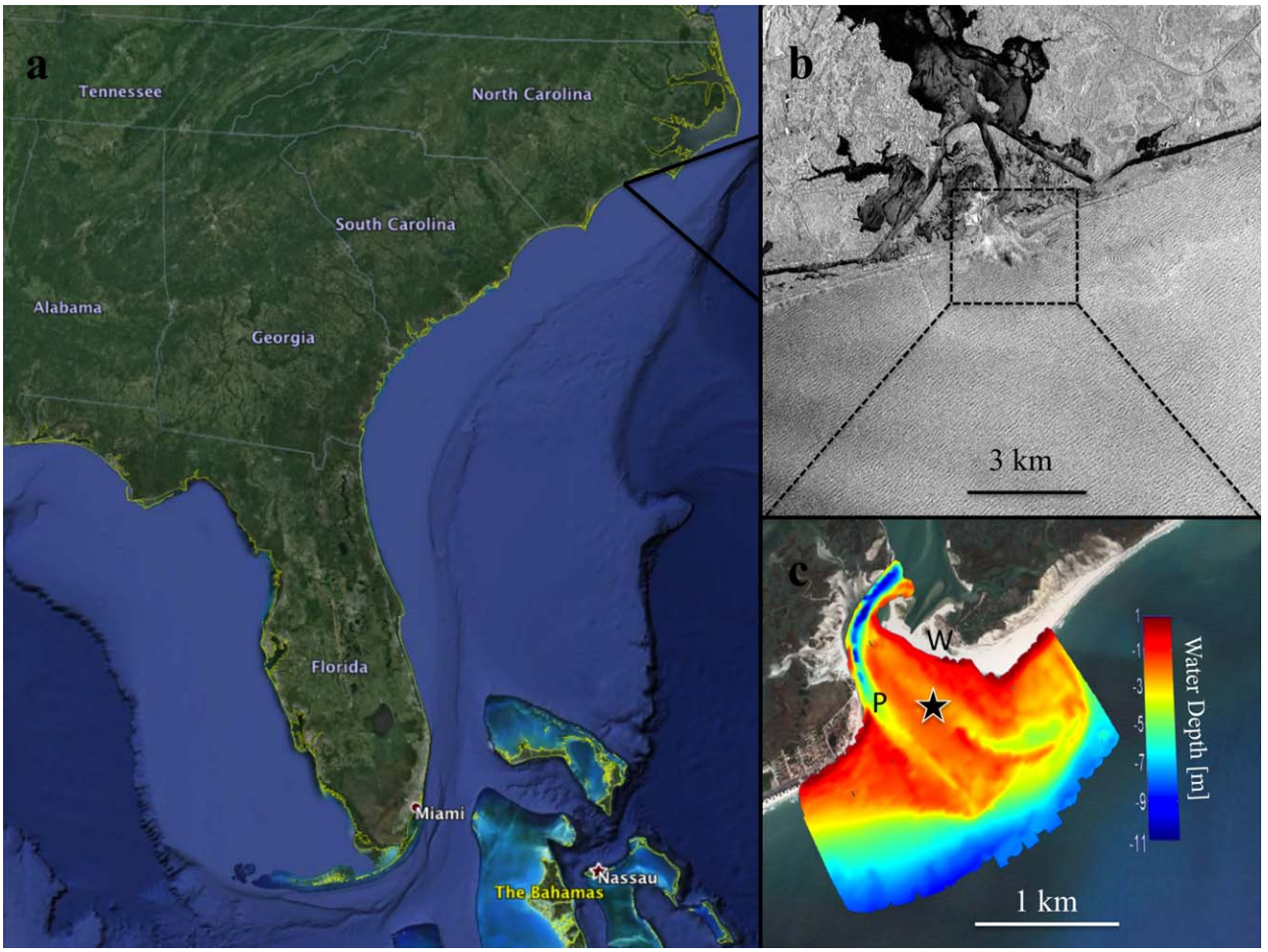

Figure 1. (a) Google Earth image of the Southeast Coast of the U.S. (b) A synthetic aperture radar (SAR) image (taken 22 May 2012) from TerraSAR-X of the inlet mouth, Intracoastal waterway, and southern end of the New River Inlet estuary, ©InfoTerra GmbH 2012. The brighter the pixels, the rougher the surface in the image. Some sort of frontal boundary is evident extending offshore of the inlet, also the white streaks nearshore indicate breaking or rapidly shoaling waves. (c) A close-up of the inlet mouth with an Army Corps of Engineers bathymetric survey overlaid, here color indicates water depth relative to the mean water level. The star marks the local origin, where the shore normal is X (increasing offshore), Y and Z follow from the right-hand rule.

77.338°W. Prior to the commencement of the experiment, the main inlet channels were dredged by the Army Corps of Engineers (Figure 1). The inlet divides North Topsail Beach to the south from Onslow Beach to the north and provides estuary-ocean exchange for the New River Estuary system and the Intracoastal Waterway. The tidal delta extends to a radius of O (1 km) [*MacMahan et al.*, 2014] and is characterized by a large ebb shoal to the south of the main channel (Figure 1). The observed tidal current range during the campaign was ±1 m/s [*Clark et al.*, 2013]. A local significant wave height range of 0.5–2 m and a wind speed range of 0–15 m/s were observed (see Figure 2) [*Wargula et al.*, 2014]. This presented an opportunity to observe wind stresses in a region with a high degree of spatial and temporal variability in both the wave and current field. Figure 1b shows a synthetic aperture radar (SAR) image taken during the RIVET experiment with significant pixel intensity variability in and around the inlet mouth. The brightness in SAR images is directly related to the surface roughness, which in turn is indicative of variability in the wind stress field at NRI.

2.2. Platform

The data presented here were collected aboard the Surface Physics Experimental Catamaran (SPEC). The motivation for developing SPEC was to transfer most of the measurement capabilities of the *Graber et al.* [2000] Air-Sea Interaction Spar (ASIS) buoy to a low-profile, mobile platform suitable for operation in the

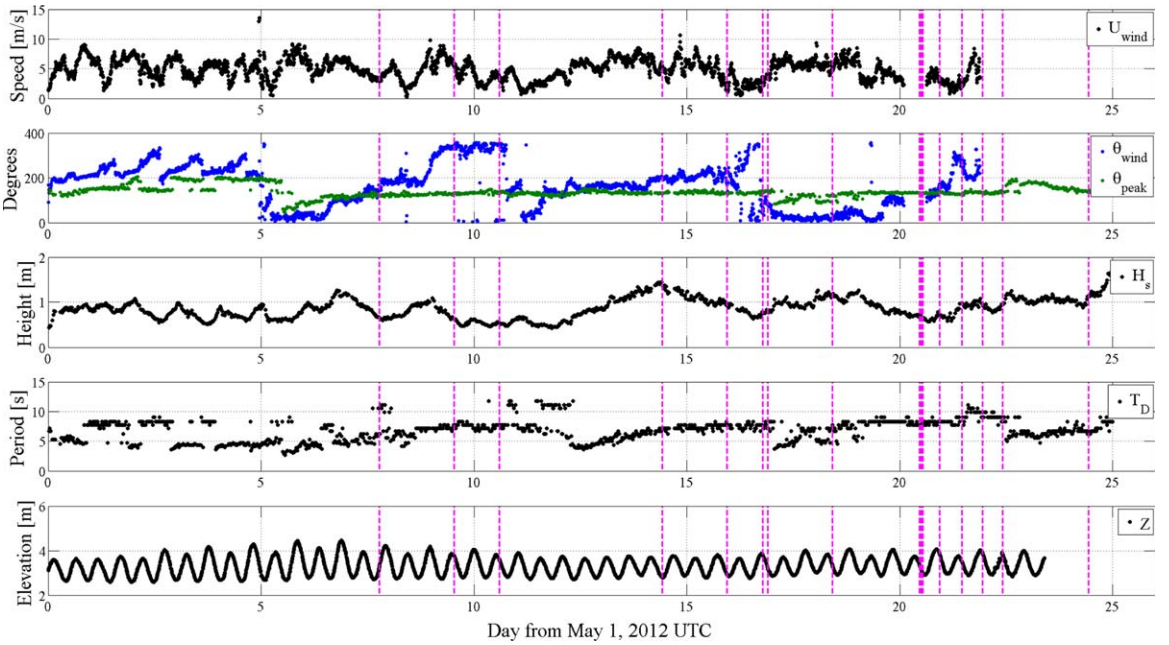

Figure 2. Time series of bulk meteorological and wave data. From top to bottom, U_{wind} is 10 min mean wind speed from an 8 m, land-based tower (location given in Figure 1c as "W"); θ_{wind} and θ_{peak} are the wind direction from the wind tower and the peak incident wave direction from an NDBC waverider buoy moored 6 km offshore of NRI, respectively; H_s is the significant wave height from the waverider; T_D is the peak period; and finally, Z is the 5 min mean water surface elevation from a bottom-mounted pressure sensor (location given in Figure 1c as "P"). All wave parameters are calculated over 30 min. Magenta lines mark start times of SPEC runs (Table 1).

inner-shelf and coastal waterways. SPEC is a converted Glacier Bay 2680 Coastal Runner that is 8.2 m long, with a 2.7 m beam and a 0.5 m draft. Some additions to the basic vessel include a 4 m tall meteorological tower and an aluminum framework mounted on the bow for near-field remote sensing and water-side measurements (Figure 3).

The meteorological mast was fitted with an ultrasonic anemometer and a probe for fast sampling of air temperature and relative humidity. The anemometer was mounted on the tower such that the sampling volume was 6.0 m above the mean water level. The bow-package included eight wave staffs, two forward-facing Acoustic Doppler Velocimeters mounted 0.5 m below the mean water line (ADVs), and a downward-facing Ultrasonic Distance Meter (UDM) positioned 0.5 m above the MWL. Custom camera mounts were also secured on the bow for infrared and polarmetric imaging. A downward-looking ADCP was mounted on the starboard-bow 0.5 m below the MWL. SPEC was deployed with two sets of accelerometers and rate gyro packages; these were used to measure the high-frequency (up to 10 Hz) vessel motions. This data are critical to recovering the momentum fluxes from the sonic anemometer.

Data from most of the sensor systems were routed via multiconductor cable into the main cabin and wired into three Campbell Scientific CR3000 dataloggers. The camera and ADCP data were captured directly to computers mounted within the SPEC cabin. An internal ethernet network and a Brandywine Network Time Protocol Server (model NTV-100RG) were used to synchronize the various acquisition clocks. The present work will focus on the 10 Hz winds from the anemometer and the 0.8 Hz profiles from the ADCP. The data analyzed in section 3 are summarized in Table 1, and an overview of conditions at NRI during the SPEC sampling is given in Figure 2. The sampling intervals roughly correspond to various satellite overflights, as well as when the flux package and the ADCP were sampling simultaneously.

2.3. Momentum Flux Calculations

Turbulent, incompressible flows can be described using the Reynolds-averaged Navier-Stokes Equation (RANS equation),

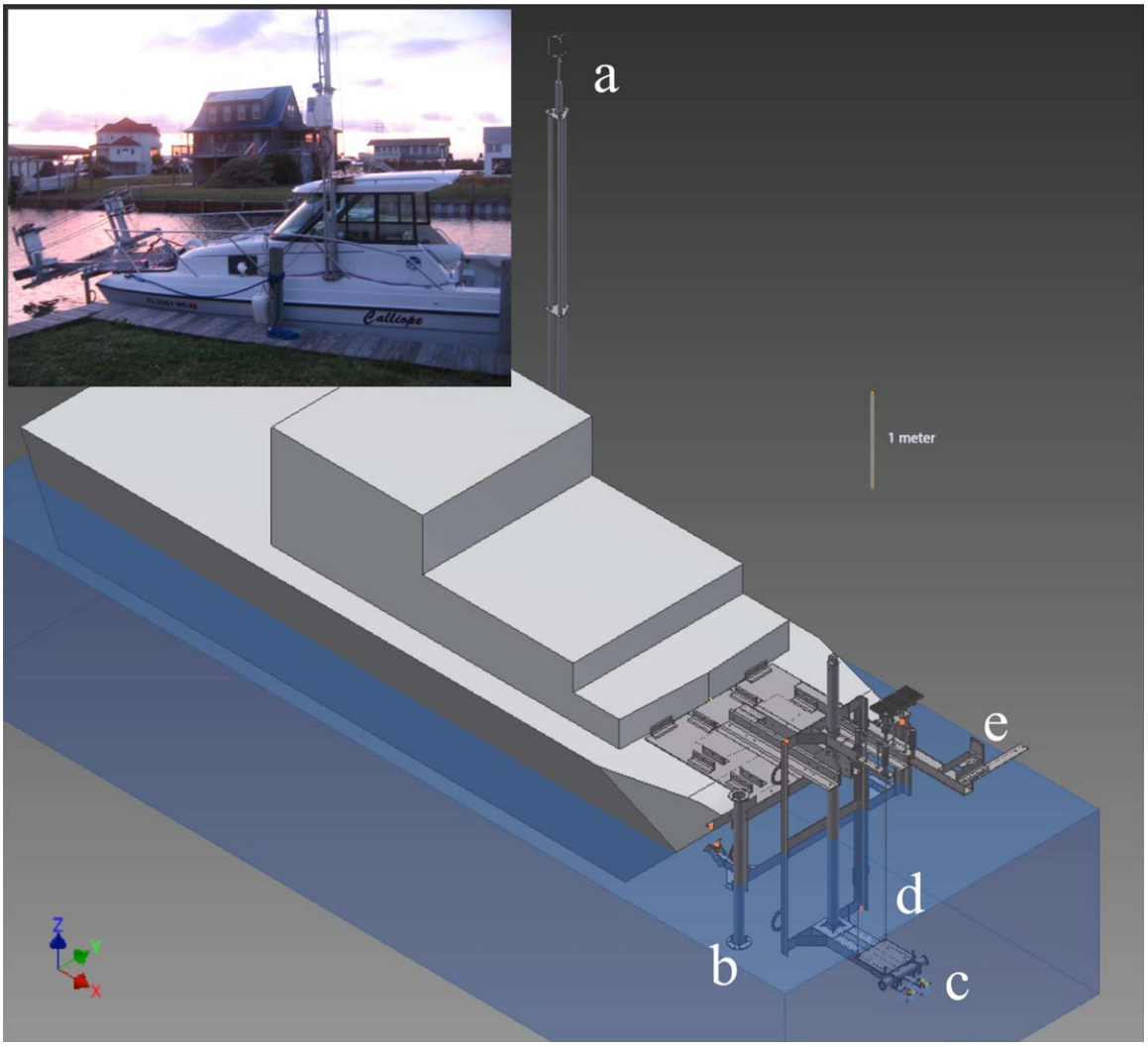

Figure 3. SPEC schematic with some instrumentation shown, see section 2.2 for more details. (a) The sonic anemometer, sampling volume located 5.99 m above the mean water level (shown in blue). Gas analyzer and high-frequency temperature and humidity probe not shown. (b) Mount for downward-looking ADCP. (c) Paired, forward-sampling ADV's. (d) Wave staff array, only two of the eight are shown. (e) Above-water mounts for polarimetric and infrared cameras and for the UDM.

$$\rho\left(\frac{\partial U_i}{\partial t}+U_j\frac{\partial U_i}{\partial x_j}\right)=F_i+\frac{\partial}{\partial x_i}\left[-P\delta_i+\mu\left(\frac{\partial U_i}{\partial x_j}+\frac{\partial U_j}{\partial x_i}\right)-\rho\overline{u_iu_j}\right] \tag{3}$$

where the instantaneous flow has been separated into its mean (U) and fluctuating (u) components. The left-hand side of equation (3) represents temporal and spatial changes in the momentum, which are balanced by the body forces and the stresses, from left to right: the mean pressure gradient, the mean strain, and the Reynolds stress [*Tennekes and Lumley*, 1972]. For wind stress analysis, it is generally assumed that over some appropriate time interval, the momentum can be considered stationary, that there is no mean advection, and that at some height above the water surface (e.g., 10 m) viscous stresses are negligible. If isotropy is invoked, and body forces are neglected, equation (3) reduces to

$$\vec{\tau}_{Total}=\vec{\tau}_{Re}=const. \tag{4}$$

where the Reynolds stress, $\vec{\tau}_{Re}$, is

$$\vec{\tau}_{Re}=-\rho_a(\overline{uw}\hat{i}+\overline{vw}\hat{j})=\vec{\tau} \tag{5}$$

Table 1. SPEC Data Used for Flux Analysis

Run[a]	Day of May	Start[b]	End	Hours	U^c	θ^d
1	8	18:45	22:15	3.5	4.57	92.20
2	10	12:40	15:45	3.08	6.88	291.7
3	11	14:15	16:45	2.5	5.28	290.3
4	15	10:05	13:00	2.92	4.80	71.54
5	16	22:30	23:50	1.33	2.41	81.07
6	17	18:30	20:20	1.83	4.39	186.0
7	17	21:00	23:30	2.5	7.62	190.8
8	19	10:10	17:40	7.5	6.92	239.7
9	21	11:00	11:55	0.92	5.82	284.5
10	21	12:00	12:50	0.83	4.65	289.4
11	21	13:00	16:55	3.92	4.61	193.9
12	21	22:25	23:40	1.25	4.30	90.89
13	22	10:55	15:25	4.5	4.67	47.79
14	22	22:40	23:59	1.33	5.33	76.60
15	23	10:00	12:20	2.33	4.45	55.24
16	25	10:20	11:35	1.25	5.23	213.8

[a]In figures, all runs are used unless explicitly noted.
[b]All times are in GMT.
[c]Mean wind speed over entire interval ref. to 10 m.
[d]Corresponding down-wind direction with respect to true north.

and [*u*,*v*,*w*] are the turbulent fluctuations of the flow aligned with the local wind direction (i.e., the along, off, and vertical wind components, respectively). The overbar represents a suitable time average. A stress angle, θ, may be defined as

$$\tan(\theta) = \overline{vw}/\overline{uw} \tag{6}$$

This angle is taken as a rotation about the vertical wind and is referenced to the mean along-wind velocity (i.e., $\theta = 0$ means the wind stress and wind velocity are in-line). The temporal mean of the vector quantities is taken prior to applying the arctangent. From equations (5) and (1), the magnitude of the wind shear velocity (or friction velocity) becomes

$$u_* = [\overline{uw}^2 + \overline{vw}^2]^{1/4} \tag{7}$$

Here the off-wind turbulent fluctuations are explicitly considered. Through the dimensional arguments made by *Monin and Obukhov* [1954], the mean wind speed profile is related to the shear velocity and a dimensionless gradient function,

$$\frac{dU}{dz} = \frac{u_*}{z\kappa}\phi_m(\zeta) \tag{8}$$

where z is the measurement elevation, κ is the Von Kármán constant, and ϕ_m is the nondimensional velocity gradient function for momentum, which is dependent on the stability parameter $\zeta = z/L$. The Monin-Obukhov Length, L, is defined as

$$L = -\frac{u_*^3\overline{\theta_v}}{g\kappa\overline{\theta_v' w}} \tag{9}$$

where $\bar{\theta}_v$ is the mean virtual temperature in air, θ_v' is the fluctuating component. By integrating equation (8), the mean wind speed as a function of height is found to be,

$$U(z) = \frac{u_*}{\kappa}\left[ln\frac{z}{z_0} - \psi_m(\zeta)\right] \tag{10}$$

where z_0 is the roughness length scale (see equation (2)) and $\psi_m(\zeta)$ is the integrated form of $\phi_m(\zeta)$. This nondimensional function corrects the logarithmic wind speed profile for non-neutral stratification [*Anctil and Donelan*, 1996]. Using equation (10) with (1), the height-dependent drag coefficient is [e.g., *Donelan*, 1990]:

$$\left(\frac{u_*}{U_z}\right)^2 = \kappa^2\left[ln\frac{z}{z_0} - \psi_m\left(\frac{z}{L}\right)\right]^{-2} \tag{11}$$

where the values for κ and the nondimensional buoyancy correction used in this study are those found in *Anctil and Donelan* [1996]. Conventionally, the drag coefficient and mean wind speed are referenced to 10 m above the air-sea interface, so that $C_z(z=10)=C_D$ and $U_{z=10}(10)=U_{10}$. *Shabani et al.* [2014] provides a detailed review of this method for deriving C_D and demonstrates its applicability to wind stresses measured over the surf zone.

2.4. Data Processing

Directly measuring the wind stress from a mobile platform (e.g., SPEC) is nontrivial and requires applying a robust postprocessing algorithm to the raw wind signals measured by the anemometer. Before applying any atmospheric corrections (see section 2.3), spikes and tilt biases must be removed. High-frequency wind records contain spikes caused by brief electronic malfunctions or other environmental factors (e.g., rain), a despiking algorithm developed by *Goring and Nikora* [2002] was used to correct the raw signals before any further processing was done.

Then using the methods developed by *Anctil et al.* [1994], the despiked wind signals were corrected for the vessel's linear and rotational accelerations (at 10 Hz). This step removes the "virtual wind" induced by the boat motion and rotates the raw winds into a station reference frame. *Edson et al.* [1991] reported that the inertial dissipation method is a viable option for retrieving fluxes from high-frequency winds that does not require boat-motion correction. However, it is generally accepted that, if the vessel motion can be quantified to high enough frequencies, the direct method is the preferred technique (see section 4 for further details).

GPS loggers, sampled at 1 Hz, were used to correct for the vessel's translational motion. GPS is sufficiently accurate for translational velocities, but the derived heading can have significant errors, especially if the vessel speed over ground is very low. Therefore, the 0.8 Hz ADCP compass data were integrated into the motion correction algorithm and used to geo-reference all the raw signals.

Another processing step that must be addressed is the averaging interval used for the analysis. The Reynolds stress is a covariance between the along and off-wind components of the turbulent velocity field and the vertical wind (equation (5)). This operation imposes some discrete time averaging interval on the data set. The amount of time that is deemed "appropriate" varies within the literature, but usually ranges from 15 to 30 min. For example, *Shabani et al.* [2014] used a 15 min averaging window, *Anctil and Donelan* [1996] used a 20 min interval, and *Potter* [2014] used 30 min for flux calculations. The assumption built-in to this approach is that either there is temporal stationarity or that Taylor's "Frozen Turbulence" hypothesis can be applied over the averaging domain. NRI posed an operationally challenging environment in this regard, as the land and sea surface were highly variable in and around the inlet mouth. In order to more meaningfully represent the variability of the wind stress observed from the moving vessel, an averaging interval of 5 min was used for the covariances. While this short averaging interval may increase the observational scatter in the wind stresses, the authors feel that, given the overarching goal of this work, this approach is justifiable modification to conventional methods. Data segments that contained large shifts in the vessel heading ($>30^{\circ}$) were not used for momentum flux estimates.

3. Results

The SPEC data set was collected between May 8 and 25, over a total of 16 individual runs of data (Table 1). During this time, 10 min mean wind speeds were observed to vary between 0 and 10 m/s, with oscillations from the southerly to the northerly directions (Figure 2). The very low frequency wind speed and direction variability (of order days) was primarily attributed to large-scale, atmospheric fronts passing through the region. The incident waves observed 6 km offshore by a directional wave rider buoy were consistently from the south, with significant wave height and mean periods of 0.5–1.5 m and 5–10 s, respectively. The majority of SPEC runs began shortly after high water, which was an operational requirement to allow for safer navigation of the NRI shoals (Figure 4).

It was consistently observed that over relatively small spatial and temporal scales, the winds in and around NRI were highly varied in both magnitude and direction. This suggested an unconventional approach to presenting the wind stress findings from SPEC. Typically, the drag coefficient is displayed with respect to wind speeds derived from equation (10) and referenced to 10 m. For the purposes of this study, the results of the wind stresses will be presented in terms of their spatial dependence, which will better reflect the in-

situ observations. A local coordinate system was used, with the origin specified as a point near the center of the inlet mouth (Figure 1). "X" is defined as the shore-normal and increasing offshore, "Y" and "Z" are found using the right-hand rule.

The normalized turbulence spectra and cospectra from SPEC are given in Figure 5. The power density spectrum from each data segment (3000 samples) were compiled and then smoothed using a centered, 30 element wide frequency bin average (i.e., the frequency domain was divided into bandwidths, each with 30 samples, and a mean power spectral density was calculated over these bands and referenced to the half-bandwidth frequency). The SPEC curves are given in natural coordinates and have been normalized by the shear velocity, u_*, squared [*Anctil and Donelan*, 1996]. *Miyake et al*. [1970] found that, when scaled correctly, measured high-frequency wind velocities exhibited a universal spectral and cospectral shape. The down-wind (S_{uu}) and vertical-wind (S_{uw}) normalized spectra, independently, show excellent agreement with both the Miyake curve and the $-5/3$ slope across the inertial subrange proposed by Kolmogorov. Note that the solid line in Figure 5 has a $-2/3$ slope, which corresponds appropriately to the Kolmogorov slope [*Miyake et al*., 1970]. The normalized cospectra of the down-wind and vertical-wind components (C_{uw}) follow the conventional curves over the low-frequency peak and the high-frequency decay. However, the observed turbulence levels are significantly higher than those presented in the Miyake curve over the frequency band between 0.2 and 1 Hz. Possible explanations for this will be discussed in the following section. It must be noted that spectral behavior such as this is not atypical of air-sea interaction studies [e.g., *Drennan et al*., 1999; *Anctil and Donelan*, 1996].

Zhang et al. [2009] showed that equations (6) and (7) are necessary in the presence of ocean surface current gradients, meaning the vector nature of the wind stress must be considered. Generally, this does not affect the conventional wind stress magnitude parameterization (Figure 6), but could affect other air-sea exchange dynamics. The across-shore distribution of wind stress angles is investigated to discern any significant trend in the stress steering off of the mean wind direction (Figure 7). A 400 m wide spatial bin average filter was applied to the 5 min mean stress angles, which were calculated from the mean across and along-wind stress components (see equation (6)). Between 0 and 1800 m across shore, there was a high propensity for wind stress steering with extreme values exceeding $\pm 70^{\circ}$. Just offshore of 2000 m there is significantly less scatter in the data, and the wind stress angle generally converges to the mean wind direction. In the furthest across-shore values, extrema are observed in the region of $\pm 50^{\circ}$.

Wind stress deviations are an inherently noisy parameter [*Edson et al*., 2013] and in order to assess the significance of the mean spatial trends observed in the across-shore distribution, student's *t* tests were used to compare three different pairs of subpopulations. Each distribution was checked for a Gaussian shape and if necessary, the methods of *Niaki and Abbasi* [2007] were used to normalize the data in order to satisfy the assumptions of the *t* test. Alpha levels were set to 0.05 for all statistical tests. The subpopulations were separated spatially, the scheme used for the statistical comparisons is given below (all distances are in meters).

$$x \leq 1000 \text{ versus } 1000 < x \leq 2000$$

$$1200 < x \leq 2000 \text{ versus } 2000 < x \leq 2800$$

$$x \leq 2000 \text{ versus } 2000 < x$$

The distribution of angles within the tidal radius of 1000 m [*MacMahan et al*., 2014] was compared to the angles between 1000 and 2000 m. A significant mean increase in wind stress deviation from the wind direction was found ($p = 0.003$). The second set of test regions was used to asses the transition in the mean wind stress deviation around the 2000 m mark. A significant ($p = 0.008$) 69% decrease in the mean wind stress angle was observed. The final test was done to investigate the degree of scatter in the furthest offshore samples, relative to the inshore data. The comparison done in this test reveals that these two particular subpopulations are not significantly exclusive ($p = 0.73$).

It has yet to be determined what processes explain the observed variability in the across-shore stress distribution. Current shear has been shown to play a major role in steering the wind stress away from the mean wind direction [*Zhang et al*., 2009]. A subset of the ADCP measured currents, observed as SPEC crossed the NRI shoals, is given in Figure 4. The spatial distribution of the current direction is shown in Figure 8, where the directions used are the near-surface current (from 1.3 m below the MWL) and the depth averaged current direction. In order to investigate stress steering, *Zhang et al*. [2009] relied on HF radar to provide two-

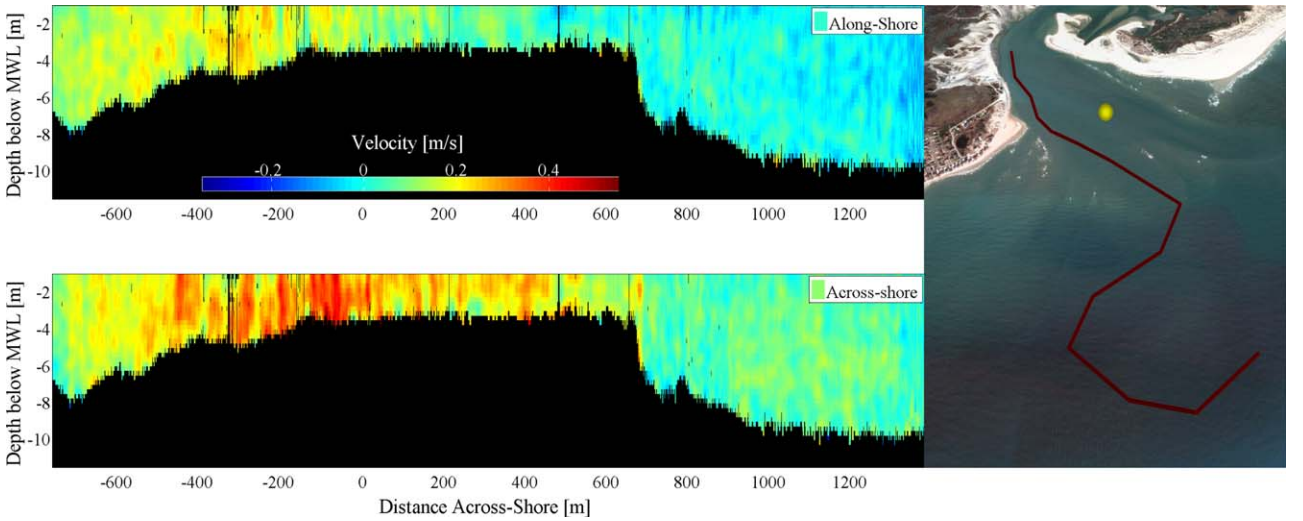

Figure 4. A sampling of the ADCP measured current profiles as SPEC crossed the NRI shoals. This data were taken from Run 13. Shown is the two-dimensional (top) alongshore and (bottom) across-shore flow velocity, where the color scale applies to both figures. On the right, the corresponding SPEC GPS track, with the (0,0) marked in yellow.

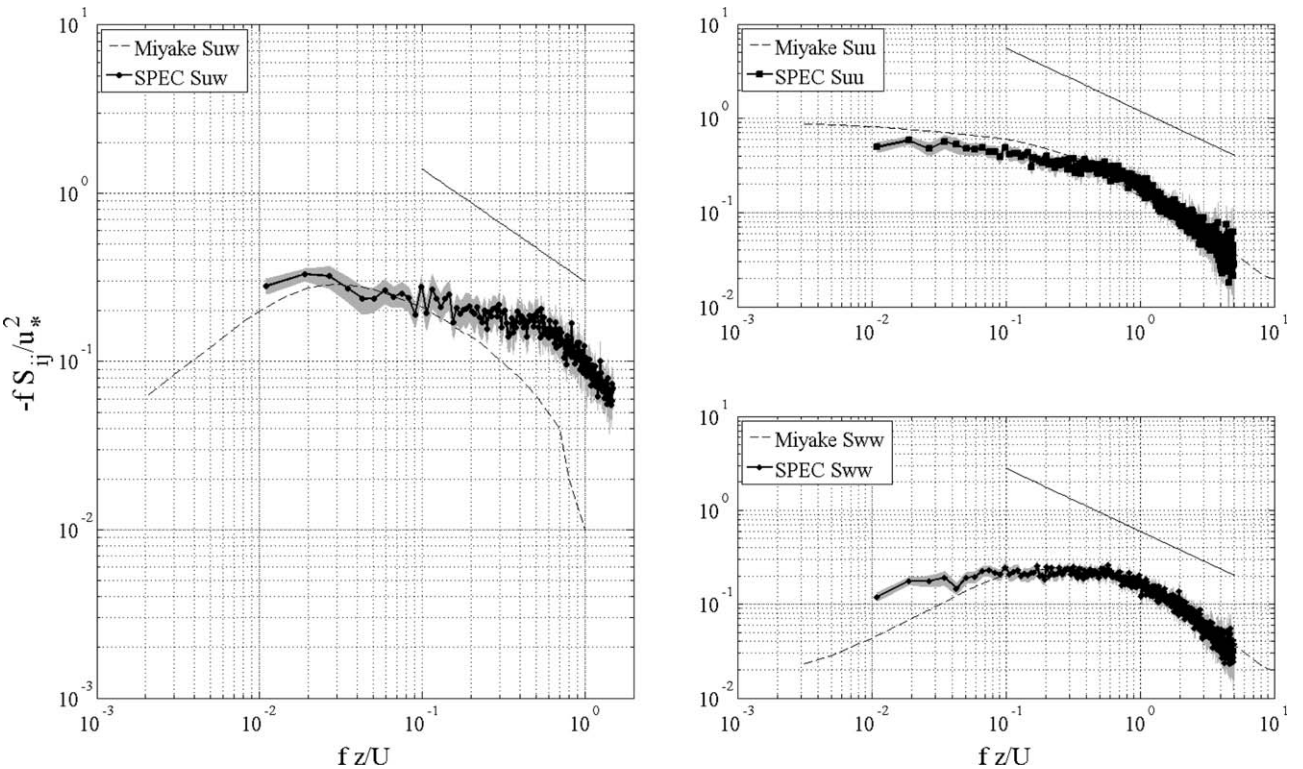

Figure 5. Turbulence spectra results compiled from all SPEC runs. The universal curves of *Miyake et al*. [1970] and the proposed Kolmogorov −5/3 slope of the inertial subrange (the thin black line) are also given. The shaded area represents the span of the 95% confidence interval calculated over a 30 element bin average. (left) The normalized cospectrum. (right) The normalized spectra for each respective component. The spectral amplitudes were normalized by the shear velocity squared, while *z* and *U* are taken as the height above the m.w.l and the corresponding mean wind speed, respectively.

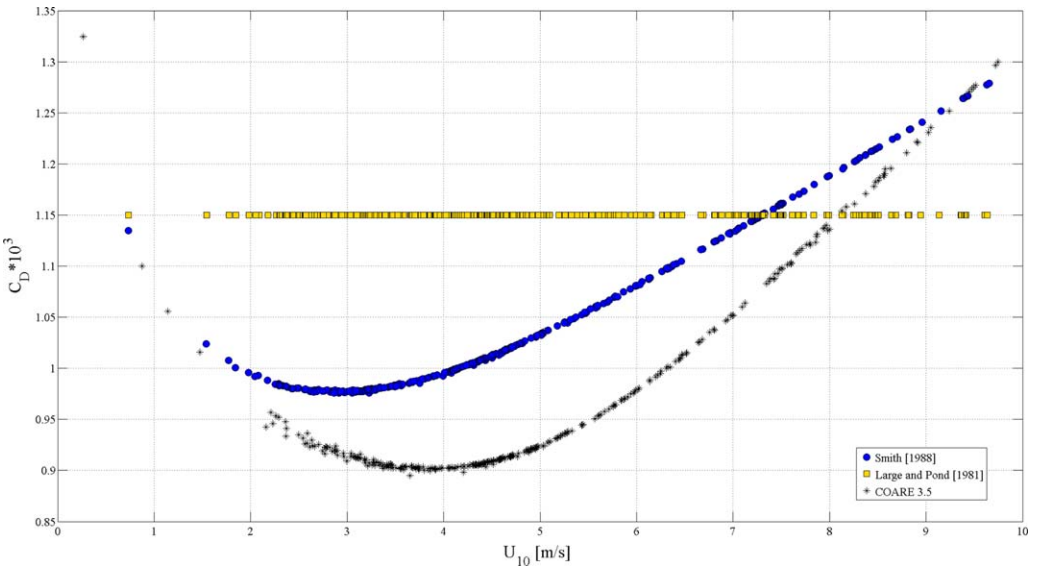

Figure 6. Three different neutral C_D parameterization algorithms using the wind velocities measured by SPEC. *Large and Pond* [1981] is piece-wise defined and remains constant for all wind speeds below 11 m/s. These algorithms were applied using equation (2) for the wind speed-dependent roughness length, z_0.

dimensional maps of the horizontal vorticity in the flow $(\frac{dU}{dy} - \frac{dV}{dx})$. The ADCP aboard SPEC cannot provide this same data, but the across-shore distribution of the 5 min mean current direction can be used as a proxy for this higher quality measurement. The same spatial averaging scheme used for the wind stress angle was applied to the ADCP data, comparisons were done between the mean trends in both variables. Qualitatively, the transitions in the spatially meaned wind stress deviation follow the current direction, especially within 2000 m of the inlet mouth; however, across the entire spatial domain, there is a weak statistical relationship between the stress angle and current direction, of O($r = 0.1$).

Another processes associated with wind stress steering is the degree of stratification in the marine boundary layer. *Geernaert* [1988] found a strong positive, linear relationship between wind stress angles and the heat flux observed from a platform in the North Sea. Following this work, the heat flux, $<wT'>$, is compared to the stress angles measured by SPEC. Here T' is the fluctuating component of the air temperature, measured by the high-frequency temperature probe on the mast. The same technique as was done to compare the stress angles to the current direction was applied to the observed heat fluxes. A statistical comparison between the stress angles and the heat flux yields a weakly positive correlation (r=0.14).

In coastal hydrodynamic modeling, the wind stress magnitude is generally parameterized by the wind speed and a nondimensional drag coefficient (equation (1)). Figure 6 provides wind stress parameterization schemes from *Large and Pond* [1981], *Smith* [1988], and *Edson et al.* [2013]. While these differ in their algorithm for calculating C_D, they remain relatively comparable over a small range of values between 0.0009 and 0.0013, for wind speeds between 0 and 10 m/s. The COARE 3.5 [*Edson et al.*, 2013] is also capable of using a sea state-dependent roughness length; however, this was not employed for this study. For simplicity, the spatial distributions of the eddy covariance measurements of the atmospheric drag are shown in relation to a *Smith* [1988] method (Figure 9). The metric used to present the results of this analysis is the dimensionless parameter R_{CD}, defined as:

$$R_{CD} \equiv \frac{C_D^{EC}}{C_D^{Smith}} \tag{12}$$

where C_D^{EC} is neutral drag coefficient directly calculated using the eddy covariance technique (see equation (11)) and C_D^{Smith} is the corresponding bulk estimate using a *Smith* [1988] algorithm. This ratio between *dimensionless coefficients* compares the direct estimate of the neutral atmospheric drag to the open ocean bulk parameterization for any given wind speed, as both quantities are calculated over the same 5 min segment of data.

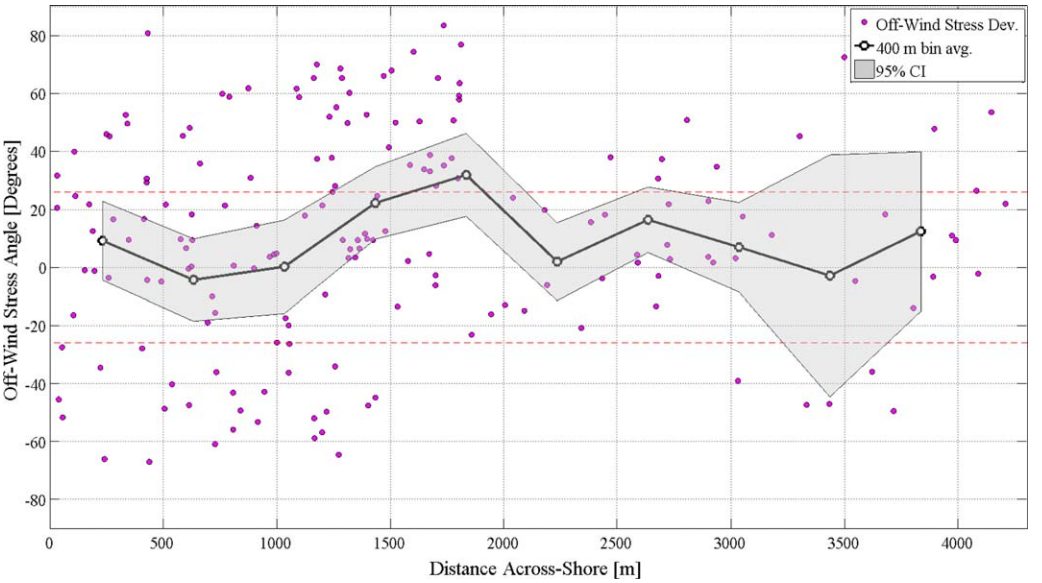

Figure 7. The spatial distribution of observed wind stress angles. The points represent the angle between 5 min means of the along and across-wind components of the wind stress. The solid line, with the open circles, gives the data filtered by a 400 m wide bin average. The shaded region spans the 95% confidence calculated from each bin. The red lines mark the $\pm 26^{\circ}$ line, which is the cutoff used in *Smith* [1980] to consider the wind stress in-line with the wind vector.

Figure 9 shows a significant degree of scatter in the calculated R_{CD} values. Generally, higher values are observed in and around the inlet mouth (i.e., near $x = 0$), while the observed variability tends to converge to the bulk estimates in the furthest offshore samples. A global average taken across all of the data yields a mean C_D 2.8 $\pm$ 0.4 times greater than the corresponding bulk estimate. The uncertainties reported here and

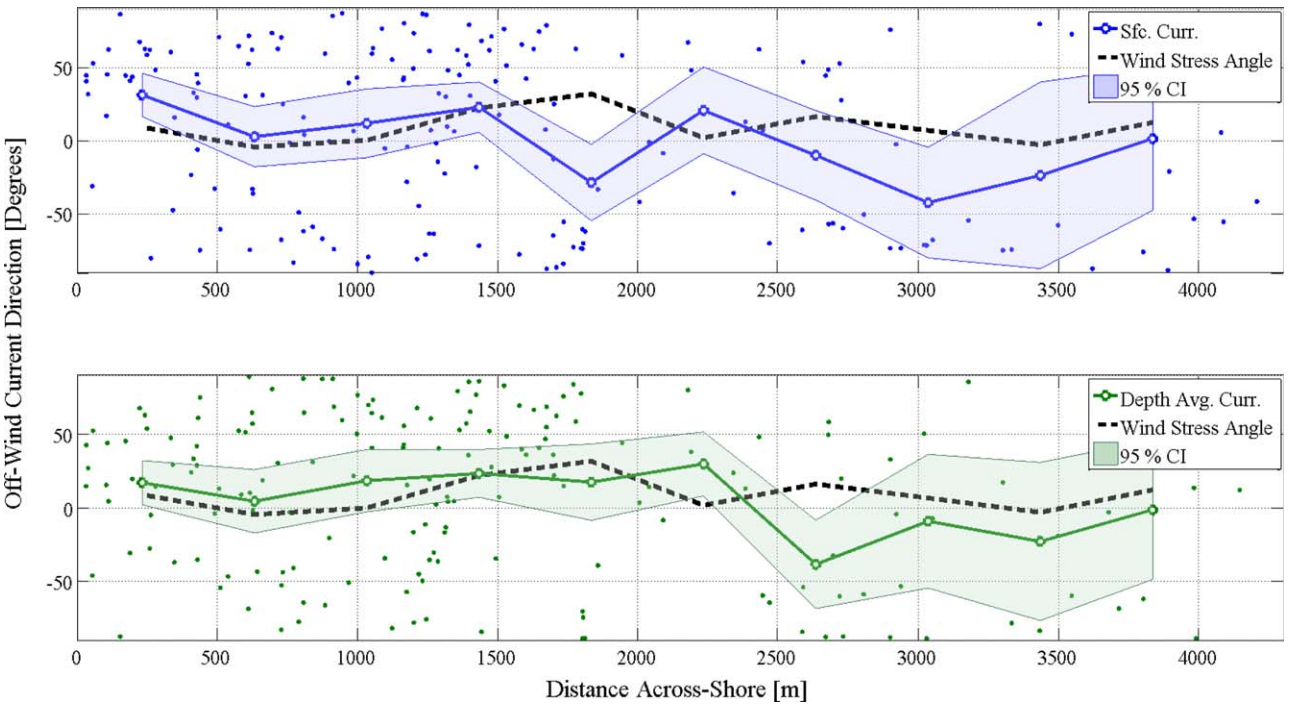

Figure 8. The spatial distribution of the (top) near-surface current direction and (bottom) depth averaged current direction as observed from the ADCP. The 5 min mean angles are shown as dots, and the same spatial filtering done in Figure 7 are shown as solid lines. In both plots, the filtered wind stress deviation from the mean wind direction is shown as a black, dashed line.

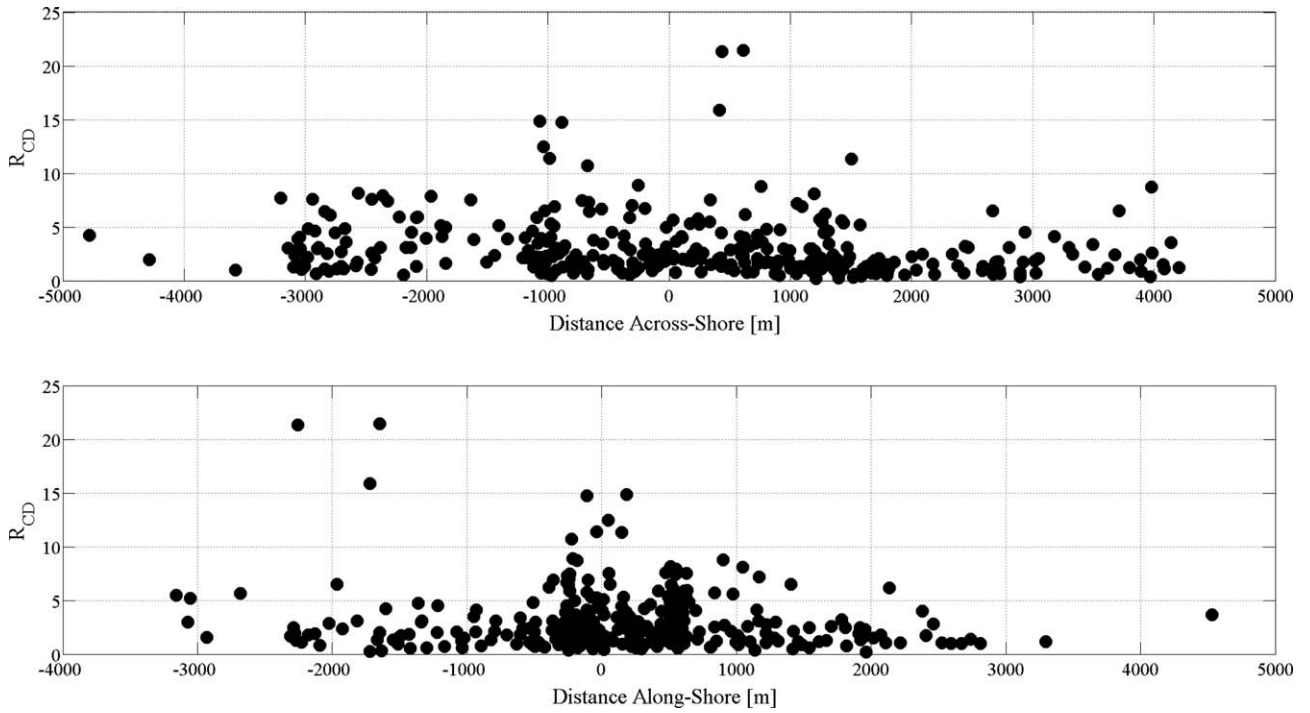

Figure 9. The (top) across-shore and (bottom) along-shore distribution of the R_{CD} values (equation (12)). Here R_{CD} is defined as the ratio of the drag coefficient calculated from an eddy covariance method to a *Smith* [1988] algorithm, for any give 5 min segment of data.

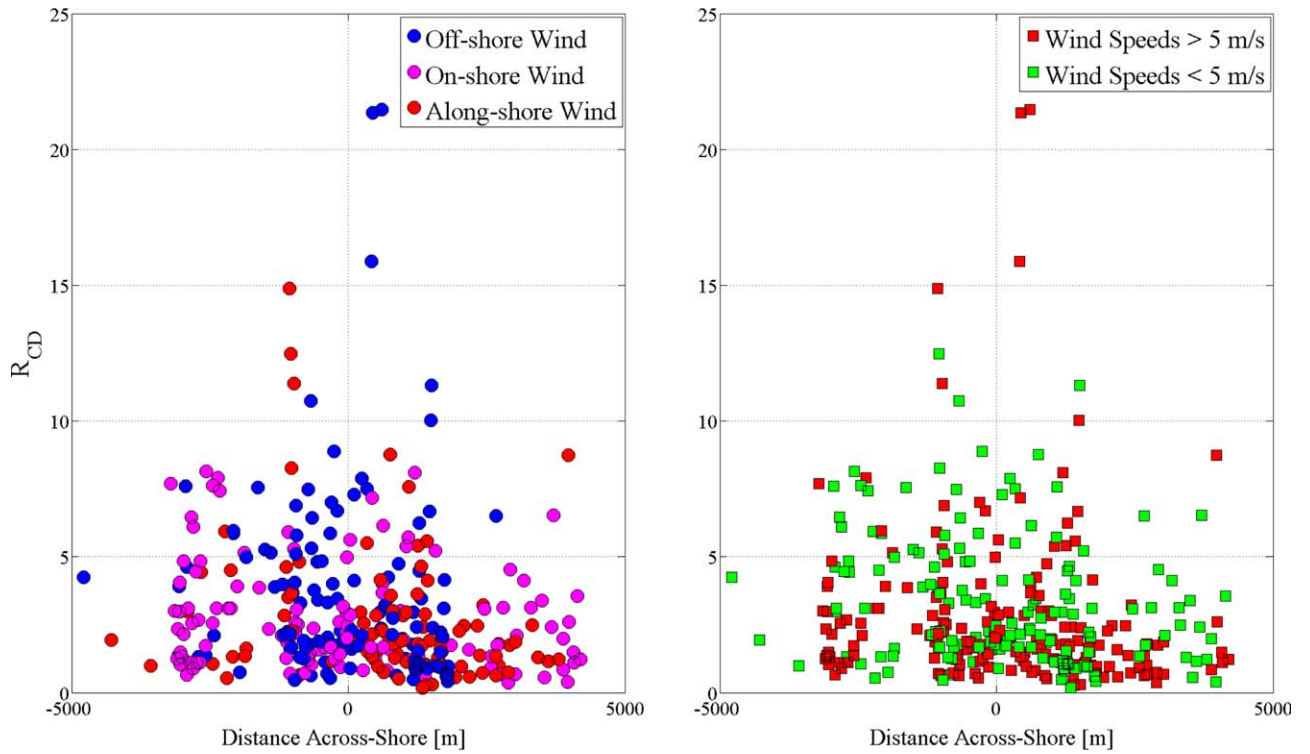

Figure 10. The same data shown in Figure 9 filtered by two different criteria: (left) wind direction and (right) wind speed. On the left, an onshore wind (magenta) is defined as a wind coming from anywhere within 45° of the shore-normal line; an alongshore wind (red) was defined as a wind coming from within 45° of the shore-parallel line. An offshore wind (blue) was defined to be 180° opposite of the onshore wind criteria. On the right, the data corresponding to wind speeds greater than 5 m/s is shown in red, while data corresponding to wind speeds less than 5 m/s is shown in green.

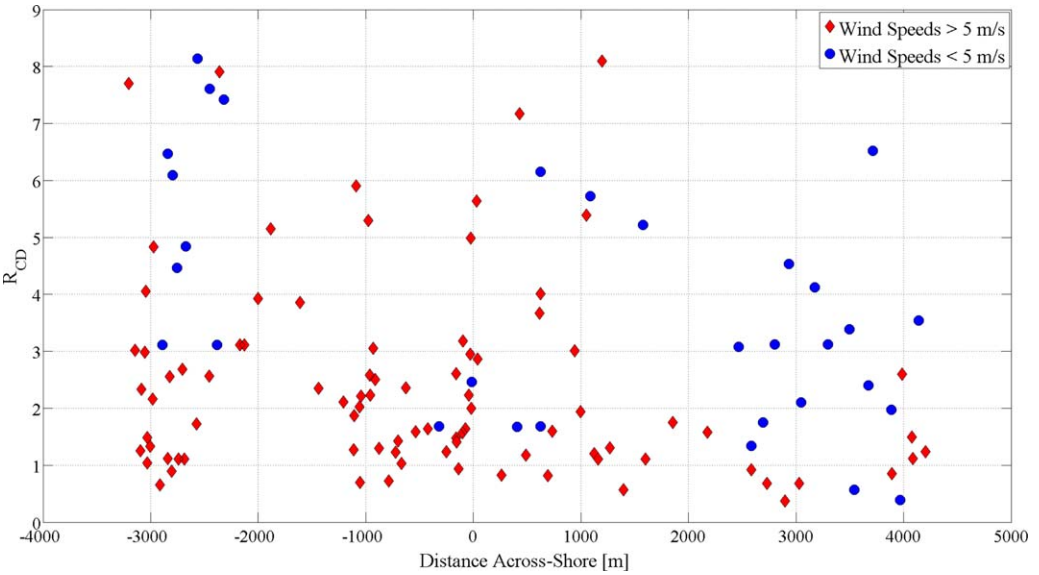

Figure 11. The cross-shore distribution of the R_{CD} value corresponding to onshore winds. The data have been separated by wind speeds above 5 m/s (black) and those below 5 m/s (white).

in the next two paragraphs are the standard error of the mean. To help explain the observed variability in the R_{CD} values, wind direction and speed filters are applied to the across-shore distribution (Figure 10).

Along coasts, wind direction has a significant effect on the nature of the atmospheric boundary layer turbulence. In an attempt to account for the complex land-air-sea effects, a three-pronged wind direction filter is utilized [*Shabani et al*., 2014]. The wind is separated into off, along, and onshore winds using the shore-parallel line as a reference. Figure 10 shows the results of this wind direction separation. The highest observed R_{CD} values occur during either offshore or alongshore winds; while, R_{CD} calculated during onshore winds do not exceed ten times the bulk drag estimate. The average R_{CD} for both offshore and alongshore winds are 3.7 ± 0.6 and 2.6 ± 0.5, respectively. The corresponding mean R_{CD} for onshore winds is 2.8 ± 0.4.

The drag coefficient has been shown to increase sharply at low wind speeds and approaching zero [*Zhu and Furst*, 2013]. To test this result on the NRI data, the R_{CD} values were filtered wind speeds greater than or less than 5 m/s (Figure 10). The mean R_{CD} for the higher wind speeds is 3.1 ± 0.5, while the mean for the lower wind speeds is 3.7 ± 0.5. Applying this wind speed filter to the onshore wind data alone shows that for winds greater than 5 m/s, the mean R_{CD} is 2.6 ± 0.5; and for onshore winds less than 5 m/s, the mean R_{CD} becomes 4.2 ± 0.7 (Figure 11). For onshore winds between 4 and 12 m/s, *Shabani et al*. [2014] observed drag coefficients roughly twice as high as conventional open ocean results. The results from SPEC for onshore winds between 5 and 10 m/s fall within 30% of these results and within 10% of the global average reported above.

4. Discussion

This work has focused on the aerodynamic drag coefficient and its stress angle with respect to the mean wind direction, because these parameters are of significant importance for coastal wave and circulation modeling. As part of this aim, the bulk of the investigations have presented in terms of the across-shore distribution. NRI divides two very similar sandy-bottomed beaches with generally parallel isobaths (Figure 1). An initial assumption given normally incident waves, as in Figure 1b, would be that the highest degree of variability in the waves, currents, winds, and topography would occur in the across-shore direction. This approach is utilized to determine the transition in the data from nearshore to a more open ocean regime. Although it is possible that the alongshore distribution could yield additional results, the scope of this study remains primarily concerned with the across-shore variability.

The departure from the Miyake cospectra shown in Figure 5 could indicate a malfunction in the instrument or processing algorithm (i.e., motion correction). However, the excellent agreement seen in S_{uu} and S_{uw}, as well as the relatively low standard errors would suggest an aerodynamic reason for this divergence. The observed air-

surface turbulence exhibits near-saturation over the frequency range 0.2–0.5 Hz, with elevated turbulence levels continuing into the high-frequency decay from 0.5 to 1 Hz. This can most likely be attributed to increased surface roughness due to wave-current interaction and/or depth-limited wave breaking and shoaling.

While, *Shabani et al*. [2014] did not provide spectral results, they attributed the increases in the observed drag to wave geometry and roughness unique to surf-zone conditions. The near-saturation and decay in turbulence observed from SPEC generally coincides with frequencies typical of nearshore waves, especially for those incidents on a highly sheared, opposing current [*Haus*, 2007]. It seems plausible that the departure from the Miyake result can be attributed to some combination of these phenomena unique to coastal processes and as yet previously undescribed from a turbulent air-sea momentum flux viewpoint. It is important to note that the high-frequency turbulent decay of all three spectra from Figure 5 follow the Kolmogorov slope, a more widely utilized metric for comparing to observed turbulent energy spectra. This is only one possible explanation, but the excellent internal consistency of the observations provides confidence in the wind stress analysis presented here.

The bulk parameterization compared to the direct estimates of C_D was implemented with a wind speed-dependent Charnock relation, i.e., the aerodynamic roughness length was assumed to be dependent on the wind shear alone. Given the nature of NRI, this may seem like a naive approach; however, it is necessary to assess the limitations of these wind stress parameterizations that have been widely deemed appropriate in the open ocean environment. While "wave field aware" versions of Charnock's relation have been established to help explain the variability in many data sets [e.g., *Yelland and Taylor*, 1996; *Drennan et al*., 1999; *Anctil and Donelan*, 1996; *Shabani et al*., 2014], an unmodified equation (2) remains the default approach to estimating the wind stress over water.

The neutral drag coefficients measured far offshore of the ebb shoals (i.e., $x > 2000$ m) generally converge to the open ocean results of *Smith* [1988], *Large and Pond* [1981], and *Edson et al*. [2013]. Additionally, in this region, the wind stress vector generally remains in-line with the wind velocity vector. This suggests that the open ocean assumptions remain a viable approach to parameterizing the wind stress for the inner-shelf while outside the influence of coastal processes, such as wave-current interaction, depth-limited breaking, and the reduction in wave celerity due to shoaling. Observations of wind stress angles and near-surface current directions show maxima near the 3500 m across-shore mark. However, this could be attributed to a lack of runs made so far offshore and could be viewed as unrepresentative of the general conditions at NRI. Further observations in this region would be necessary to confirm that this trend is in fact characteristic and not an episodic event captured by SPEC.

The wind stress angle variability was compared directly to the horizontal current shear and the air-sea heat fluxes, both of which have been shown to steer the wind stress off of the mean wind azimuth [*Geernaert*, 1988; *Zhang et al*., 2009]. Wave shoaling is another possible factor, but could not be considered here. The area covered by the moving platform in conjunction with the high spatial variability of the wave field at NRI rendered the wave-stress coupling analysis outside the realm of the present work. The current direction was found to be weakly correlated with the wind stress angle. However, if only data inshore of 1800 m is considered, the correlation becomes stronger ($r = 0.72$, for the near-surface current direction). Similar results are found for the depth averaged currents. This region coincides with the strongest current gradients (e.g., Figure 4) and studies have shown that the presence of strong, horizontal current gradients contribute to the wind stress steering [*Haus*, 2007]. This result suggests that the stress-current coupling is inhomogeneous around NRI and that specific spatial scales are important when considering these dynamics.

Cross-correlation analysis was done to further investigate the spatial relationship between the wind stress and these variables. Again, considering region inshore of 1800 m, the strong relationship between the stress angle and the near-surface current was confirmed at the zero lag. However, in regards to the heat flux (for the entire across-shore domain), a strong linear relationship was found with the stress angle at the $+1$ lag, which corresponds to a 400 m interval. Clearly, the horizontal current shear and atmospheric stratification play a significant role in steering the wind stress, however the exact mechanism for this remains obscure. The NRI outflow plume is assumed to be the primary source of horizontal variability in both variables and separating these contributions to the stress steering is beyond the scope this study.

The eddy covariance technique is a well-established method in air-sea interaction research and was used here to parameterize the atmospheric drag. The inertial dissipation method is another means of extracting drag coefficient estimates from high-frequency wind data [e.g., *Large and Pond*, 1981; *Edson et al*., 1991;

Table 2. Global Mean R_{CD} Value With Varying Time Averaging Intervals

Minutes	Meters Traveled by SPEC[a]	Mean	$\pm SEM$[b]
5	300	2.8	0.4
10	600	2.9	0.4
15	900	3.3	0.6
20	1200	3.4	0.6
25	1500	3.4	0.6

[a]Assumes a vessel speed over ground of 1 m/s.
[b]One standard error of the means.

Yelland and Taylor, 1996]. This method relies on Kolmogorov's hypothesis of the universal shape of the turbulence spectrum of the down- wind component of the velocity over the inertial subrange. From *Yelland and Taylor* [1996], the turbulent dissipation rate, ϵ, is related to the measured wind velocity, U, by,

$$S_{uu}(f) = K\varepsilon^{2/3} f^{-5/3} (U/2\pi) \tag{13}$$

where K is the Kolmogorov constant, f is the measurement frequency, and $S_{uu}(f)$ is the frequency-dependent power spectral density converted from wave number using Taylor's "Frozen Turbulence" hypothesis. The inertial dissipation technique has advantages over the eddy covariance method in that it does not require motion correction, is less sensitive to flow distortions, and it is not contingent on a specific temporal averaging interval.

The authors found that the same calculations made using the inertial dissipation method were highly variable and depended primarily on the frequency interval used to integrate $S_{uu}(f)$ from equation (13). Although, inertial dissipation has proved useful for a significant amount of air-sea flux research, the observed inconsistencies in the results discouraged its use for the analysis presented in this work.

For SPEC, the careful design of the platform rendered significant flow distortion a non-issue. Also, the *Anctil et al*. [1994] method applied to the raw winds successfully removed any tilt biases due to the vessel motions (which in contrast to typical open ocean measurements were relatively small). Table 2 shows the effect of increasing averaging interval on the global mean R_{CD} value. The results are found to be consistent up to a twenty-five minute averaging interval. The increases in the standard error of the means with increasing averaging interval is most likely indicative of decreasing sample size, rather than some physical process.

Runs were discretized into 5 min segments, over which all calculations were made, including the mean wind speed and direction, the Reynolds stresses, and the shear velocity. The motivation for this was to more accurately represent the wind stress across the tidal inlet—this may be emphasized through flux footprint analysis. The flux footprint can be defined as the two-dimensional surface area of roughness elements upwind of some measurement point, that contribute to the flux measured at some height, z, above the surface [see *Högström et al*., 2008; *Schuepp et al*., 1990]. An up-wind distance, x_{max}, can be defined such that it represents the distance from the sensor to the largest contribution to the flux. From *Schuepp et al*. [1990], this can be related to the measured wind by,

$$x_{max} = \frac{U}{u_*}\frac{z}{2\kappa} \tag{14}$$

where U is the wind speed, u_* is the shear velocity, and κ is the Von Kármán constant. The magnitude of this one-dimensional footprint is inversely proportional to the amount of turbulence generated up-wind, i.e., short distances for rough surfaces (breaking waves and houses) and longer distances for smooth surfaces (deep-water waves). *Högström et al*. [2008] reported two-dimensional flux areas from 10^4 to 10^7 m^2 for winds measured over the open ocean. Flux footprints measured at NRI are relatively smaller than these observations, but order of magnitude variability within runs was typically measured (Figure 12). The land-sea surface changes the flux footprint dramatically in and around the inlet and the short time averaging window used for this study helps to better represent the wind stress field at NRI.

5. Conclusions

The goal of this study was to evaluate the efficacy of open ocean wind stress parameterization methods in predicting the observed stresses at NRI, to attempt to explain the variability in the in situ data, and to augment the limited collection of coastal observations focused on air-sea interaction processes. To first order, the open ocean methods underestimate the atmospheric drag by a factor of 2.6; and the general assumption that the wind stress is in-line with the wind velocity vector is only reliable off-shore of 2 km from NRI. In and around the tidal inlet, observed wind stresses significantly diverge from the previous work, with the

10 m drag exceeding 20 times the bulk method prediction and wind stress deviations from the mean wind azimuth occasionally surpassing $\pm 70^{\circ}$. This suggests that uniquely coastal processes, such as strong current gradients, wave shoaling, and depth-limited breaking, are misrepresented in the open ocean algorithms. The wind direction (relative to the shoreline) and low wind speed conditions were successfully used to explain the majority of the variability in the eddy covariance-derived drag coefficients. The near-surface, horizontal current shear was used to explain a significant amount of the observed stress angle variance near the inlet mouth. The observed ambiguity in the role the heat flux plays in the stress steering highlights the significance of atmospheric stratification in these boundary layer processes.

Further investigation is needed to characterize the dynamics of wind-wave-current coupling in shallow water, as this has the potential to better represent the air-sea forcing. Specifically, the effect that the nearshore wave field has on the wind stress vector must be explicitly determined. Additionally, the effect of strong, horizontal gradients in the currents and stratification needs to be analyzed. Future work will focus on these topics. Determining the impact that these findings have on coastal model performance is required to assess the wider applicability of these results. Numerical model studies into coastal processes rely on open ocean algorithms to simulate the wind forcing [*Roelvink and Reniers*, 2011]. Adapting simulations to a coastally appropriate wind model will be a necessary next step to better understanding nearshore air-sea interaction. The inherent physical complexity of coastal waters encourages novel methods and techniques to further air-sea interaction study in the nearshore.

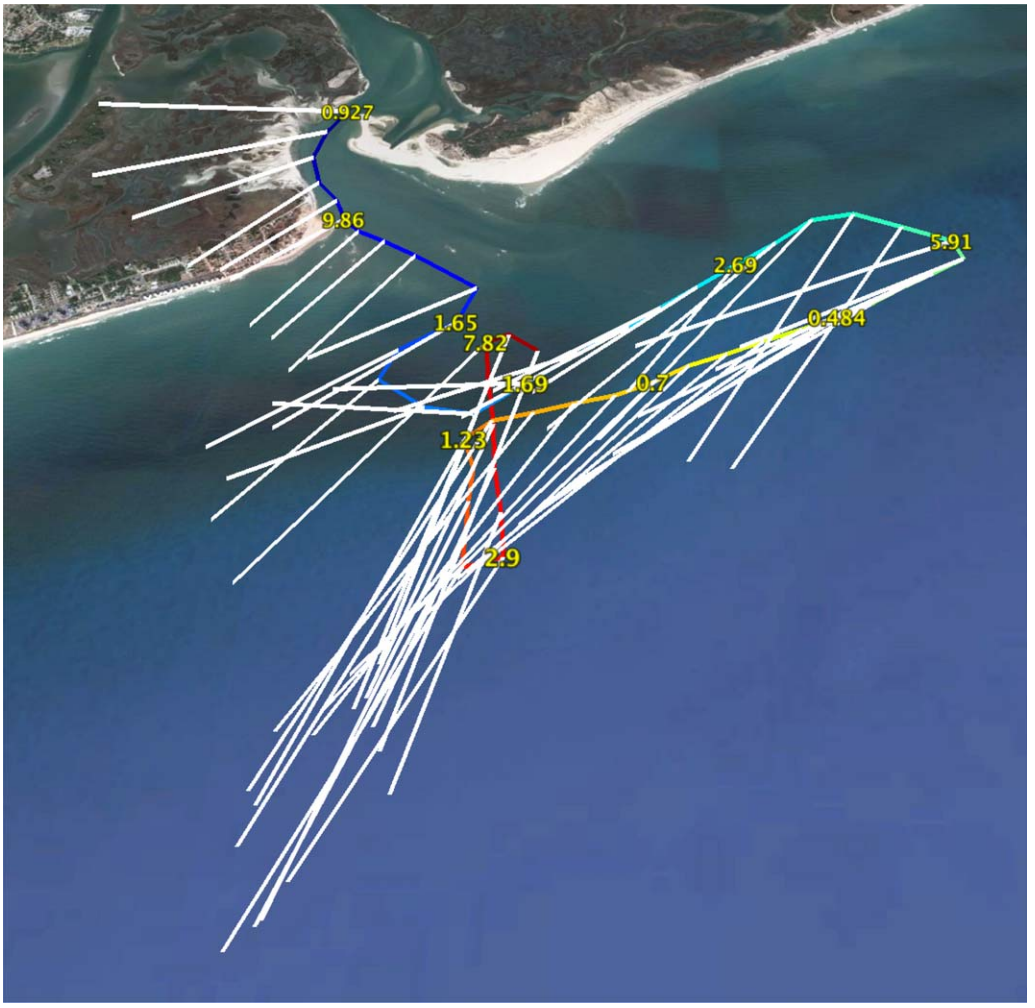

Figure 12. The one-dimensional flux footprints along the SPEC GPS track for Run 13. There is one white "stick" for each 5 min segment of fluxes, they are all oriented up-wind. The spatial coverage of each stick was calculated using equation (14). The colored line corresponds to the SPEC GPS, where the color represents time since start of run: blue is the beginning, red is the end. The numeric labels are select neutral drag coefficients observed along the track.

Acknowledgments

This work was supported by the Office of Naval Research through research grants N000141410643, N000141310144, N000141210448, N000141010409, and N000141010379. Additional support came from GOMRI, via the CARTHE Consortium grant SA1207GOMRI005. Field experiments require the combined effort and dedication of an entire cohort, the authors would like to give a special thank you to Mike Rebozo and Rafael Ramos for their valuable contributions throughout this project. Britt Raubenheimer and Steve Elgar are thanked for providing the water surface elevation data. The authors would like to thank Eric Terrill and his group for providing the land-based wind tower data. Jamie MacMahan is thanked for logistical support and the use of his docking facility during the RIVET I field campaign. Clarence O. Collins III and Henry Potter, of the Naval Research Laboratory, are appreciated for their helpful commentary and suggestions. The counsel of William Drennan during the data processing and analysis was also greatly appreciated. Additional efforts made by two anonymous reviewers were instrumental in improving the quality of this article. The data and computational scripts used are securely stored at the University of Miami's Rosenstiel School of Marine and Atmospheric Science campus and can be made available upon request, please direct inquiries to the corresponding author or to bhaus@rsmas.miami.edu.

References

Anctil, F., and M. A. Donelan (1996), Air-water momentum flux observations over shoaling waves, *J. Phys. Oceanogr.*, *26*, 1344–1353.

Anctil, F., M. A. Donelan, W. M. Drennan, and H. C. Graber (1994), Eddy-correlation measurements of air-sea fluxes from a Discus Buoy, *J. Atmos. Oceanic Technol.*, *11*, 1144–1150.

Ardhuin, F., T. H. C. Herbers, K. P. Watts, G. Ph. van Vledder, R. Jensen, and H. C. Graber (2007), Swell and slating-fetch effects on wind wave growth, *J. Phys. Oceanogr.*, *37*, 908–931.

Charnock, H. (1955), Wind Stress on a water surface, *Q. J. R. Meteorol. Soc.*, *81*, 639–640.

Clark, D. B., L. Lenain, F. Feddersen, E. Boss, and R. T. Guza (2013), Aerial imaging of fluorescent dye in the near shore, *J. Atmos. Oceanic Technol.*, *31*, 1410–1421.

Donelan, M. A. (1990), Air-sea interaction, in *The Sea, vol. 9, Ocean Engineering Science*, edited by B. LeMehaute and D. M. Hanse, pp. 239–292, Wiley-Interscience, Hoboken, N. J.

Donelan, M. A., B. K. Haus, N. Reul, W. J. Plant, M. Stiassnie, H. C. Graber, O. B. Brown, and E. S. Saltzman (2004), On the limiting aerodynamic roughness of the ocean in very strong winds, *Geophys. Res. Lett.*, *31*, L18306, doi:10.1029/2004GL019460.

Drennan, W. M., H. C. Graber, and M. A. Donelan (1999), Evidence for the effects of swell and unsteady winds on marine wind stress, *J. Phys. Oceanogr.*, *29*, 1853–1864.

Edson, J. B., C. W. Fairall, P. G. Mestayer, and S. E. Larsen (1991), A study of the inertial-dissipation method for computing air-sea fluxes, *J. Geophys. Res.*, *96*, 10,689–10,711.

Edson, J. B., V. Jampana, R. A. Weller, S. P. Bigorre, A. J. Plueddemann, C. W. Fairall, S. D. Miller, L. Mahrt, D. Vickers, and H. Hersbach (2013), On the exchange of momentum over the open ocean, *J. Phys. Oceanogr.*, *43*, 1589–1610.

Feng, Z., A. J. H. M. Reniers, B. K. Haus, and H. M. Solo-Gabriele (2013), Modeling sediment-related enterococci loading, transport, and inactivation at an embayed nonpoint source beach, *Water Resour. Res.*, *49*, 693–712, doi:10.1029/2012WR012432.

Fujimura, A., A. J. H. M. Reniers, C. B. Paris, A. L. Shanks, J. H. MacMahan, and S. G. Morgan (2014), Numerical simulations of larval transport into a rip-channeled surf zone, *Limnol. Oceanogr.*, *59*, 1434–1447.

Garratt, J. R. (1977), Review of drag coefficients over oceans and currents, *Mon. Weather Rev.*, *105*, 915–929.

Geernaert, G. L. (1988), Measurements of the angle between the wind vector and wind stress vector in the surface layer of the North Sea, *J. Geophys. Res.*, *93*, 8215–8220.

Goring, D. G., and V. I. Nikora (2002), Despiking acoustic doppler velocimeter data, *J. Hydraul. Eng.*, *128*, 117–126.

Graber, H. C., E. A. Terray, M. A. Donelan, W. M. Drennan, J. C. Van Leer, and D. B. Peters (2000), ASIS—A new air-sea interaction spar buoy: Design and performance at the sea, *J. Atmos. Oceanic Technol.*, *17*, 708–720.

Haus, B. K. (2007), Surface current effects on the fetch-limited growth of wave energy, *J. Geophys. Res.*, *112*, C03003, doi:10.1029/2006JC003924.

Högström, U., et al. (2008), Momentum fluxes and wind gradients in the marine boundary layer—A multi-platform study, *Boreal Environ. Res.*, *13*, 475–502.

Kitaigorodskii, S. A., and Y. A. Volkov (1965), On the roughness parameter of the sea surface and the calculation of momentum flux in the near-water layer of the atmosphere, *Izv. Acad. Sci. USSR Atmos. Oceanic. Phys., Engl. Transl.*, *1*, 973–988.

Large, W. G., and S. Pond (1981), Open ocean momentum flux measurements in moderate to strong winds, *J. Phys. Oceanogr.*, *11*, 324–336.

MacMahan, J., J. van de Kreeke, A. J. H. M. Reniers, S. Elgar, B. Raubenheimer, E. Thornton, M. Witmer, P. Rynne, and J. Brown (2014), Fortnightly tides and subtidal motions in a choked inlet, *Estuarine Coastal Shelf Sci.*, *150*, 325–331, doi:10.1016/j.ecss.2014.03.025.

Miyake, M., R. W. Stewart, and R. W. Burling (1970), Spectra and cospectra of turbulence over water, *Q. J. R. Meteorol. Soc.*, *96*, 138–143.

Monin, A. S., and A. M. Obukhov (1954), Basic laws of turbulent mixing in the surface layer of the atmosphere, *Tr. Akad. Nauk SSR Geohiz. Inst.*, *24*(151), 163–187.

Niaki, S. T. A., and B. Abbasi (2007), Skewness reduction approach in multi-attribute process monitoring, *Commun. Stat. Theory Methods*, *36*, 2313–2325.

Potter, H. (2014), A study of turbulent processes at the air-sea interface in high winds, PhD thesis, pp. 251, Univ. of Miami, Coral Gables, Fla.

Roelvink, J. A., and A. J. H. M. Reniers (2011), *A Guide to Modelling Coastal Morphology, Advances in Coastal and Ocean Engineering*, vol. 12, World Sci., London, U. K.

Sahleé, E., W. M. Drennan, H. Potter, and M. A. Rebozo (2012), Waves and air-sea fluxes from a drifting ASIS buoy during the Southern Ocean Gas Exchange experiment, *J. Geophys. Res.*, *117*, C08003, doi:10.1029/2012JC008032.

Schuepp, P. H., M. Y. Leclerc, J. I. MacPherson, and R. L. Desjardins (1990), Footprint prediction of scalar fluxes from analytical solutions of the diffusion equation, *Boundary Layer Meteorol.*, *50*, 355–373.

Shabani, B., P. Nielsen, and T. Baldock (2014), Direct measurements of wind stress over the surf zone, *J. Geophys. Res. Oceans*, *119*, 2949–2973, doi:10.1002/2013JC009585.

Smith, S. D. (1980), Wind stress and heat flux over the ocean in gale force winds, *J. Phys. Oceanogr.*, *10*, 709–726.

Smith, S. D. (1988), Coefficients for sea surface wind stress, heat flux, and wind profiles as a function of wind speed and temperature, *J. Geophys. Res.*, *93*, 15,467–15,472.

Smith, S. D., and E. G. Banke (1975), Variation of the sea surface drag coefficient with wind speed, *Q. J. R. Meteorol. Soc.*, *101*, 665–673.

Tennekes, H., and J. L. Lumley (1972), *A First Course in Turbulence*, MIT press, Cambridge, Mass.

Wargula, A., B. Raubenheimer, and S. Elgar (2014), Wave-driven along-channel subtidal flows in a well-mixed ocean inlet, *J. Geophys. Res. Oceans*, *119*, 2987–3001, doi:10.1002/2014JC009839.

Yelland, M., and P. K. Taylor (1996), Wind stress measurements from the open ocean, *J. Phys. Oceanogr.*, *26*, 541–558.

Zhang, F. W., W. M. Drennan, B. K. Haus, and H. C. Graber (2009), On wind-wave-current interactions during the Shoaling Waves Experiment, *J. Geophys. Res.*, *114*, C01018, doi:10.1029/2008JC004998.

Zhu, P., and J. Furst (2013), On the parameterization of surface momentum transport via drag coefficient in low-wind conditions, *Geophys. Res. Lett.*, *40*, 2824–2828, doi:10.1002/grl.50518.